International Journal of Thermal Sciences 159 (2021) 106606

Contents lists available at ScienceDirect

International Journal of Thermal Sciences

journal homepage: http://www.elsevier.com/locate/ijts

Instability characteristics of a highly separated natural convection flow: Configuration of a tandem of cold and hot horizontally oriented cylinders placed within a cold cubic enclosure

Efi Zemach [b], Avihai Spizzichino [a,c], Yuri Feldman [a,*]

[a] Department of Mechanical Engineering, Ben-Gurion University of the Negev, P.O. Box 653, Beer-Sheva, 84105, Israel
[b] Department of Mechanical Engineering, Shamoon College of Engineering, Beer-Sheva, 84100, Israel
[c] Soreq NRC, Yavne, 81800, Israel

ARTICLE INFO

Keywords:
Natural convection
Preserving and breaking the flow symmetry
Slightly bifurcated flow regime
Hopf bifurcation

ABSTRACT

The study numerically investigated the instability characteristics of a 3D highly separated natural convection flow developing within a cold cubic enclosure in the presence of a tandem of hot and cold horizontally aligned cylinders. The immersed boundary (IB) method was utilized to enforce kinematic no-slip and thermal boundary conditions on the surfaces of the two cylinders. The obtained results were based on the analysis of slightly supercritical flows simulated for three different distances between the cylinders and for Rayleigh numbers $Ra \propto O(10^6)$. It was found that the transition to unsteadiness of the flow sets in via the first Hopf bifurcation, which preserves two types of reflectional symmetry with respect to the central cross-section of the cubic enclosure. The impact of the closeness of the cavity boundaries to the cylinder surfaces on the quantitative and qualitative characteristics of the observed instabilities was extensively investigated. The study elucidated the fundamental instability characteristics typical of highly separated thermally driven flows in confined containers in terms of the bifurcation characteristics and the impact of the object orientation and closeness to the container boundaries on preserving the spatio-temporal symmetries of the slightly supercritical flow.

1. Introduction

Highly separated laminar and turbulent flows are ubiquitous in various engineering applications. Separation of external and internal flows determines the overall performance of many engineering devices, including airfoils, gas and water turbines, pumps, pipelines, and various types of heat exchanger, to name but a few. Typical unsteady turbulent separated flows are characterized by variations in time and in the spatial location of separation and reattachment points, as well as by the occurrence of secondary separation regions. In addition, the flow regime is markedly affected by the shape of obstacles immersed in the bulk flow, by stochastic fluctuations of the turbulent flow, and by various instability mechanisms. As a result, quantitative investigation of the characteristics of highly separated flows constitutes a challenging task.

The most significant progress in the investigation of highly separated external flows has been made in the field of aerospace engineering. In this field, focus was directed to the investigation of force generation for wings and airfoils undergoing unsteady motions (e.g., pitching, flapping, and accelerating) and to revealing the correlation between the dynamics of the wake vortices [1] and unsteady aerodynamic forces (see, e.g. Ref. [2,3]). In contrast, the investigation of highly separated internal flows was motivated by the need to characterize the thermally driven flows developing in vertical channels equipped with fins of various shapes and conductivities, with the aim to facilitate the manipulation and control of the heat transfer rate from the channel side walls [4–7]. In channels with perfectly insulating fins, only the wall regions close to the reattachment points of the flow are characterized by an enhanced heat flux rate compared to the walls of an entirely smooth channel. Such perfectly insulating fins will, however, increase the hydraulic resistance of the flow, which, in turn, will slow the flow and decrease the heat transfer rate. In contrast, the flow developing in the presence of fins of high thermal conductivity will be characterized by an abrupt increase in the heat flux on the channel surface in the vicinity of the fin and on the fin surface itself [8–10].

A deeper insight into the impact of the separation phenomenon on the characteristics of thermally driven flows has been acquired from the investigation of flow regimes developing within tall vertical channels [4,

* Corresponding author.
E-mail address: yurifeld@bgu.ac.il (Y. Feldman).

https://doi.org/10.1016/j.ijthermalsci.2020.106606
Received 9 February 2020; Received in revised form 20 August 2020; Accepted 21 August 2020
Available online 13 September 2020

Nomenclature

Roman Symbols

$\boldsymbol{u}$	velocity vector
u_x	velocity component in x direction
u_y	velocity component in y direction
u_z	velocity component in z direction
p	pressure
t	Time
Ra	Rayleigh number, $Ra = \frac{g\beta}{\nu\alpha}\Delta TL^3$
Pr	Prandtl number, $Pr = \frac{\nu}{\alpha}$
D	cylinder diameter
L	length of the cavity side
T	temperature, [K]
$\overrightarrow{g}$	gravity acceleration
$\overrightarrow{e}_z$	unit vector in z direction
$\overline{Nu}$	surface averaged Nusselt number
$\boldsymbol{f}$	volumetric force
q	volumetric heat flux
L_∞	infinity norm

Greek Symbols

Θ	temperature
ω	angular frequency
ν	kinematic viscosity, [m^2 /s]
α	thermal diffusivity, [m^2 /s]
β	coefficient of thermal expansion, [$1/K$]
ρ	density of the fluid, [kg/m^3]
δ	distance between the cylinder centers
h	hot
c	cold

Subscripts

k	$k-th$ Lagrangian point of immersed surface
0	ambient

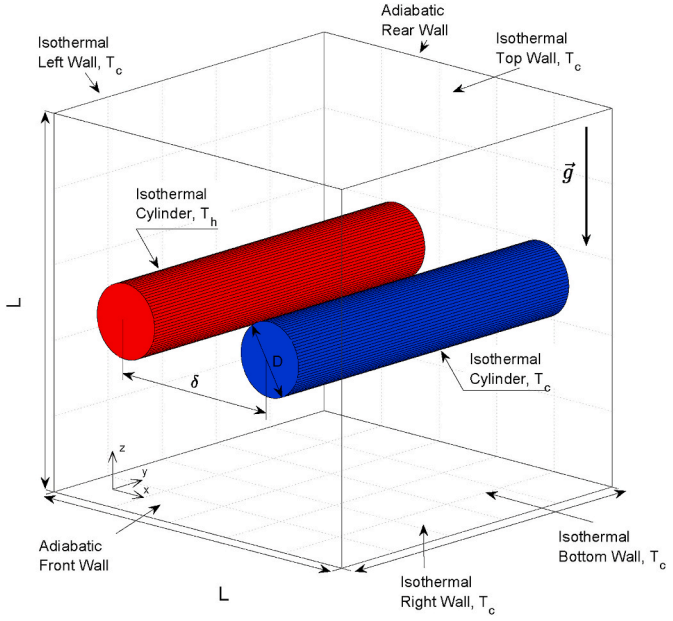

Fig. 1. Physical model of a tandem of hot and cold cylinders horizontally aligned inside a cold cube.

6,11] with horizontal fins and within square and cubic cold cavities containing immersed obstacles in the form of one [12–15] or more [16–20] hot horizontal cylinders. The investigation of natural convection flow within cold cubic enclosures containing horizontal hot cylinders is, specifically, of theoretical interest, as it is possible to obtain highly separated periodic flows at a Ra value as small as $\sim 10^5 \div 10^6$ (see e.g. Ref. [21]). Such flows can be simulated by the direct solution of Navier–Stokes (NS) equations without the need to introduce turbulence modeling. Remarkably, the natural convection flow developing within such a configuration is generated by temperature gradients, which coincide with the direction of the gravity force, and the flow is, therefore, unconditionally unstable. If the cubic cavity hosts both cold and hot cylinders, the unstable flow will typically separate as a result of the interaction between oppositely directed hot and cold plumes rising and descending from the surfaces of the hot and cold cylinders, respectively. Confined natural convection flow in the presence of cylinders of various shapes and orientations is a rapidly developing field that is not exclusively restricted to Newtonian flows. The recent interest in the field has been extended to Carreau and viscoplastic fluids [22,23] and to flows driven by both thermal and magnetohydrodynamic forces [24]. These recent studies have shed light on the impact of entropy generation and of the strength of the magnetic field on heat and mass transfer rates.

In our recent study [21], the instability characteristics of natural convection flow developing in the presence of a tandem of vertically aligned hot and cold cylinders placed within a cold cubic container were investigated. In that study, the complex structure of the dynamics of the bulk flow was characterized both quantitatively and qualitatively. Special emphasis was placed on revealing the impact of the vertical distance between the hot and the cold cylinders, as well as on investigating the impact of the cavity boundaries on the characteristics of the slightly supercritical flow. The present work aims to further investigate the fundamental mechanisms determining the dynamics of slightly supercritical highly separated natural convection confined flows. In particular, the natural convection flow generated within a cold cubic cavity in the presence of a tandem of horizontally aligned hot and cold cylinders is considered. In this scenario, the interaction of two oppositely directed thermal plumes in the central region of the cavity gives rise to the formation of a fully 3D, highly separated, thermally driven flow. The study investigates two different instabilities characterizing a flow undergoing a transition to unsteadiness, including the symmetry preserving phenomenon and the spatial structure of the leading perturbations. The present work thus constitutes an important milestone in building the comprehensive picture necessary to fully characterize the physical mechanisms determining the onset of instability of natural convection flows generated by a tandem of hot and cold horizontally oriented cylinders of different orientations and different distances, one from the other.

2. Theoretical background

In common with our previous study [21], we again investigate the heat transfer patterns and the flow surrounding the immersed objects. The cubic cavity shown in Fig. 1 is the same as that in our previous study (with the front and back walls being adiabatic and all the other walls being held at constant temperature). However, in contrast to our previous work, the immersed objects are horizontal (not vertical) identical cylinders, one maintained at a cold temperature, T_c, and the other at a hot temperature, T_h. The cylinder centers are separated by a distance δ, as shown in Fig. 1. Following our previous work [21], the same value of the ratio between the cylinder diameter, D, and the length of the cavity side, L, equal to $D/L = 0.2$, is taken. The following NS and energy

Table 1
Geometry characteristics of the sphere in cube configurations used for the validation study.

R_i/a	L/a	L/R_i	$Nu_L = f(Ra_L)$[28]
0.43	0.40606	1.89	$Nu_L = 0.578Ra_L^{0.239}$
0.67	0.28702	0.86	$Nu_L = 0.388Ra_L^{0.249}$
0.86	0.1978	0.45	$Nu_L = 0.384Ra_L^{0.231}$

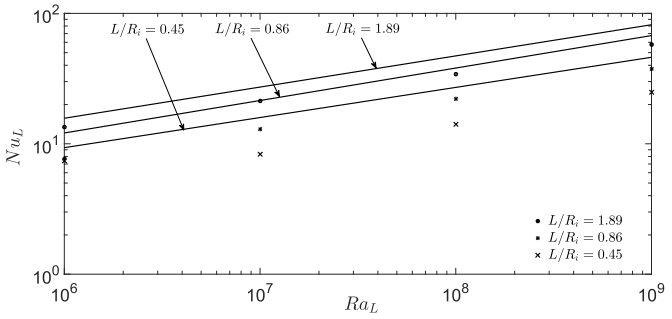

Fig. 2. Comparison between the current (discrete points) and the experimentally obtained values [28] (solid lines) of Nu_L as a function of Ra_L.

equations governing the natural convection flow can be rendered non-dimensional, as in Ref. [25]:

$$\nabla \cdot \boldsymbol{u} = 0, \tag{1}$$

$$\frac{\partial \boldsymbol{u}}{\partial t} + (\boldsymbol{u} \cdot \nabla)\boldsymbol{u} = -\nabla p + \sqrt{\frac{Pr}{Ra}}\nabla^2 \boldsymbol{u} + \theta \vec{e}_z + \boldsymbol{f}, \tag{2}$$

$$\frac{\partial \theta}{\partial t} + (\boldsymbol{u} \cdot \nabla)\theta = \frac{1}{\sqrt{PrRa}}\nabla^2 \theta + q, \tag{3}$$

where $\boldsymbol{u} = (u,v,w)$, p, t and θ are the non-dimensional velocity, pressure, time and temperature, respectively, and the gravity force acts in the opposite direction to the $\vec{e}_z$ unit vector. The flow is assumed to be Newtonian and incompressible. The Boussinesq approximation is employed to address the buoyancy effects, i.e., the energy and the momentum equations in the z direction are coupled through the temperature source term θ resulting from the assumption $\rho = \rho_0(1 - \beta(T - T_c))$, where ρ_0 is the air density measured at temperature T_c. No turbulence modeling is introduced, as all the simulations are performed for relatively moderate values of the Rayleigh number ($O(10^6)$) and at a sufficiently small value of the time step ($\Delta t = 10^{-3}$), such that all the spatio-temporal flow scales are fully resolved by the direct numerical simulations. The viscous dissipation is neglected. The effect of the immersed objects on the surrounding flow is resolved by employing the immersed boundary (IB) method. As a result, the volumetric force $\boldsymbol{f}$ and the volumetric heat flux q appear as source terms in the momentum and energy equations, respectively. IB method solves the problem on the structured grid which allows taking an advantage of existing very efficient numerical algorithms, e.g. Ref. [26], utilized as a driver in the currently implemented method. The flow is determined by two non-dimensional groups, namely, the Prandtl number, $Pr = \nu/\alpha$, and the Rayleigh number, $Ra = \frac{g\beta}{\nu\alpha}\Delta T L^3$, where ν is the kinematic viscosity, α is the thermal diffusivity, β is the isobaric coefficient of thermal expansion of the working fluid, g is the value of gravitational acceleration, and $\Delta T = T_h - T_c$ is the temperature difference between the hot and cold cylinders. The non-dimensional groups are obtained by utilizing L, $U = \sqrt{g\beta L\Delta T}$, $t = L/U$, and $P = \rho_0 U^2$ as scales for length, velocity, time and pressure, respectively. The Pr value is taken throughout to be 0.71, since the medium is air. We next define the Nusselt number, Nu, as the ratio of convective to conductive heat fluxes from the given surface. The local Nu value is equal to the non-dimensional surface heat flux Q, which in accordance with the scaling utilized in the present study should be multiplied by the factor $\sqrt{PrRa}$ (see Eq. (3)) and also by a non-dimensional grid size Δz to convert the local volumetric heat flux to its surface counterpart. Since the uniform cartesian grid $\Delta x = \Delta y = \Delta z$ is utilized throughout this study, the average value $\overline{Nu}$ for the surface of each cylinder can be calculated by:

$$\overline{Nu} = \sqrt{PrRa}\Delta x \overline{Q}. \tag{4}$$

Here, the average heat flux $\overline{Q}$ is calculated by taking the arithmetic mean of all the non-dimensional heat fluxes Q_k, intrinsically calculated by the solution of the system of Eqs. (1)–(3) at each Lagrangian point k of the corresponding cylinder surface.

Eqs. (1)–(3) are solved by utilizing the semi-implicit direct forcing IB method recently developed in Ref. [15], in accordance with which, the volumetric $\boldsymbol{f}$ and q sources introduced into the governing equations (1)–(3) are solved implicitly. The detailed description of the method, applied to the simulation of the natural convection flows falling within the scope of the present study, is presented in our previous paper [21] and is therefore not repeated here for the sake of brevity. The validation, verification and grid independence studies relevant to the presently investigated configurations are given in the next sections. We note in passing that the algorithm utilized here is based on the distributed Lagrange multiplier approach as means to enforce kinematic constraints for velocity and temperature on the cylinder surfaces and employs the SIMPLE method to obtain the divergence-free velocity field. The standard second-order finite volume method [27] is utilized for discretization of all the spatial derivatives, while a second-order backward difference scheme is utilized for the time discretization. The algorithm consists of precomputing and time integration steps [15]. All the results reported here were calculated on both 200^3 and 300^3 grids with the aim to prove the grid independence of the obtained results. All the simulations were performed on a standard Linux server containing 24 cores (48 threads) and 128 Gb RAM. The total time required to complete a typical simulation depends strictly on a grid resolution. Details are given below.

3. Validation study

The developed numerical methodology was validated by comparison of the numerically obtained results with the experimental data provided

Table 2
Comparison between the present study and the previously published values [18] (as measured by photogrammetry of the corresponding charts) for $\overline{Nu}$, averaged over the surface of a hot cylinder placed within a cold cube and $\overline{Nu}_G$, averaged over the surface of the cold cube as appears in Ref. [21].

	$Ra = 10^4$				$Ra = 10^5$				$Ra = 10^6$			
	Nu		Nu_G		Nu		Nu_G		Nu		Nu_G	
R/L	Ref. [18]	Current	Ref. [18]	Current	Ref. [18]	Current	Ref. [18]	Current	Ref. [18]	Current	Ref. [18]	Current
0.1	6.2493	6.4880	1.0201	1.0208	11.138	11.662	1.8099	1.8360	18.3260	19.2500	2.9945	3.0348
0.2	5.1184	5.1500	1.6161	1.6188	7.2271	7.5800	2.3766	2.3814	13.3610	13.9370	4.3985	4.3677
0.3	5.8084	5.7304	2.6216	2.9091	6.4790	6.5169	2.9726	3.0702	11.2720	11.4010	5.1956	5.3844
0.4	8.7030	8.5544	5.1919	5.3928	8.7030	8.7643	5.2651	5.5131	10.7160	10.8320	6.6106	6.8313

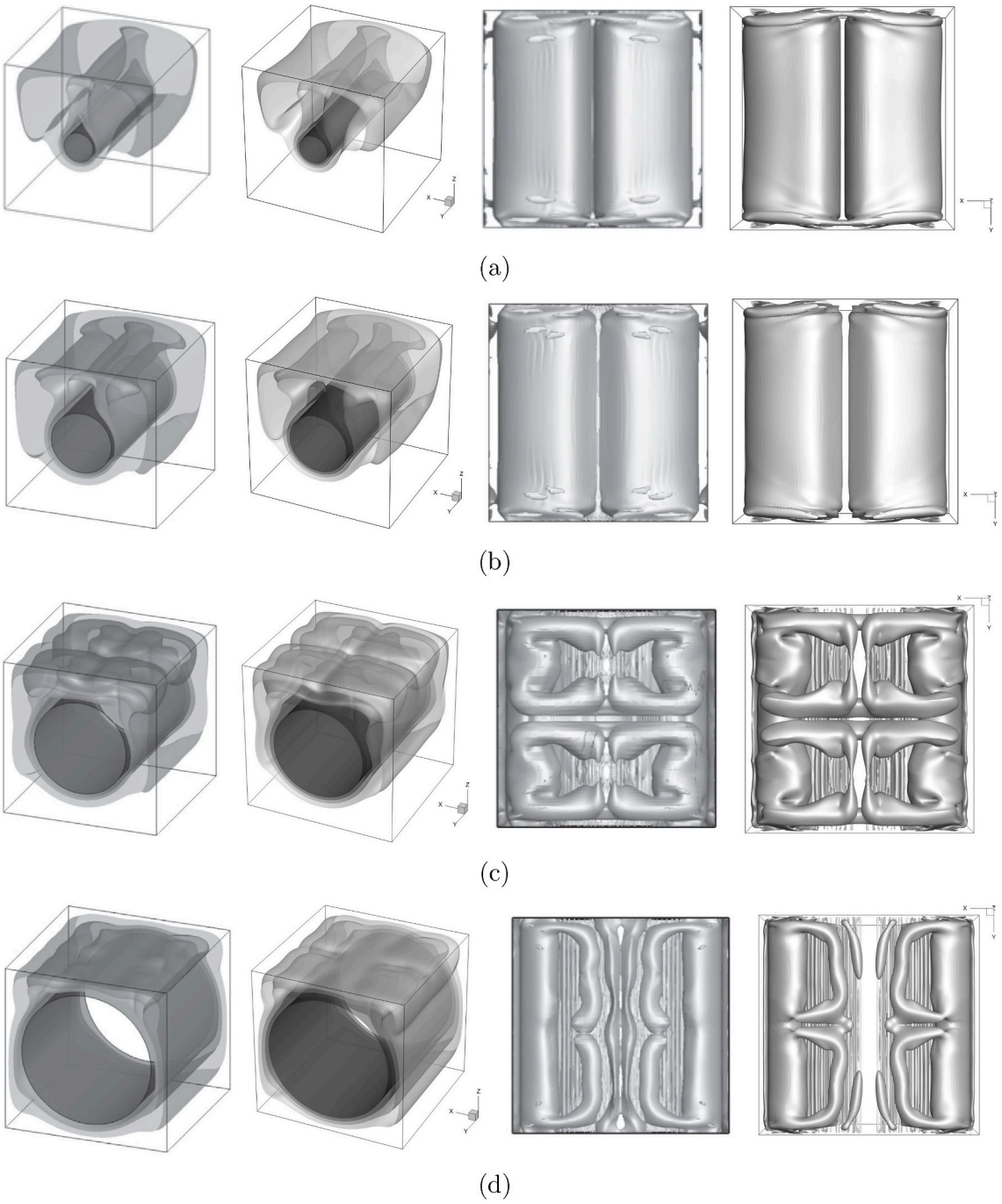

Fig. 3. Comparison of the iso-contours of temperature (first pair of columns: the left column presents the results reported in Ref. [18], and the right column presents the currently obtained results) and of the iso-surfaces of the $\lambda_2 = -0.1$ criterion (second pair of columns: the left column presents the results reported in Ref. [18], and the right column presents the currently obtained results). The results were obtained for $Ra = 10^6$ and for: (a) $R/L = 0.1$; (b) $R/L = 0.2$; (c) $R/L = 0.3$; (d) $R/L = 0.4$.

Table 3
Coordinates of points at which the temperature evolution was acquired.

Point No.	X	Y	Z
P1	0.25	0.4875	0.25
P2	0.25	0.4875	0.75
P3	0.75	0.4875	0.25
P4	0.75	0.4875	0.75
P5	0.25	0.5125	0.25
P6	0.25	0.5125	0.75
P7	0.75	0.5125	0.25
P8	0.75	0.5125	0.75

in Ref. [28] for the natural convection heat transfer between hot bodies confined by an isothermal cold enclosure. In particular, the configuration of a hot sphere placed at the center of a cold cubic container was chosen. The results are given in terms of the values of the Nusselt number Nu_L as a function of the Rayleigh Ra_L number. The subscript L means that both values are based on the length scale $L = R_o - R_i$, where R_o is the radius of an equivalent spherical enclosure having the same volume as the cold cubic container, and R_i is the radius of the sphere. According to the above scaling and denoting the length of the cubic container side as a (to be consistent with the nomenclature utilized in Ref. [28]) the value of Ra_L can be related to the value of Ra introduced in

Table 4
Maximal and minimal values of the Nusselt numbers $\overline{Nu}_c$ and $\overline{Nu}_h$, averaged over the surfaces of the cold and hot cylinders, respectively, together with the value of ω corresponding to the angular frequency of the leading harmonics as a function of δ. The calculations were performed on 200^3 and 300^3 uniform structured grids.

	$max(\overline{Nu}_c)$		$min(\overline{Nu}_c)$		$max(\overline{Nu}_h)$		$min(\overline{Nu}_h)$	
δ/ Grid	200^3	300^3	200^3	300^3	200^3	300^3	200^3	300^3
0.4	−2.973	−2.986	−2.974	−2.988	30.803	30.892	30.788	30.879
0.5	−3.397	−3.417	−3.423	−3.443	30.861	30.949	30.824	30.918
0.6	−3.236	−3.245	−3.317	−3.327	21.266	21.322	21.194	21.248

Table 5
Maximal and minimal values of the temperature θ monitored at control points P4, P2 and P1 (see Table 3) as a function of δ. The calculations were performed on 200^3 and 300^3 uniform structured grids.

	$\delta = 0.4$				$\delta = 0.5$				$\delta = 0.6$			
	θ_{max}, P4		θ_{min}, P4		θ_{max}, P2		θ_{min}, P2		θ_{max}, P1		θ_{min}, P1	
Grid	200^3	300^3	200^3	300^3	200^3	300^3	200^3	300^3	200^3	300^3	200^3	300^3
	0.2901	0.2913	0.2878	0.2892	0.5702	0.5677	0.5304	0.5270	0.01939	0.01947	0.01921	0.01928

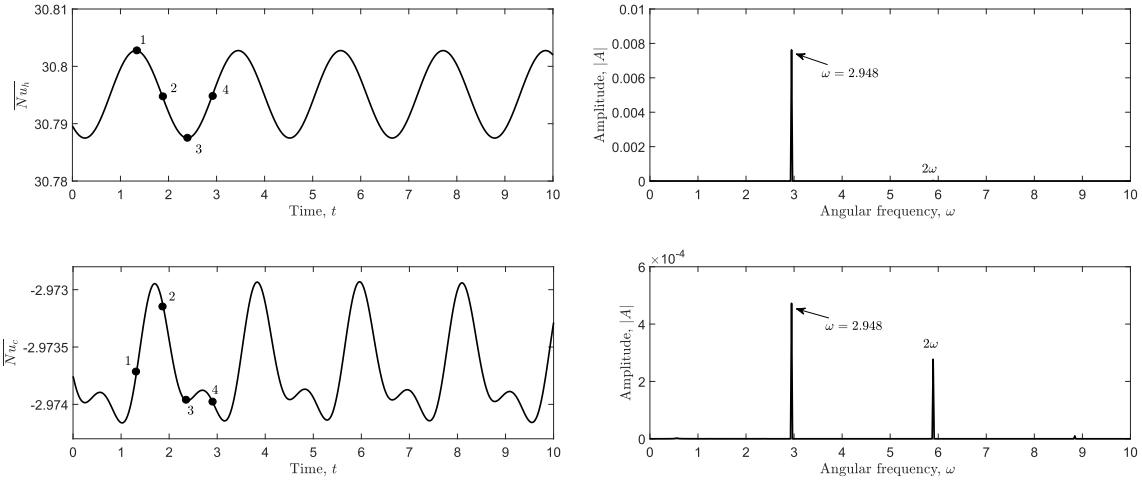

Fig. 4. Time evolution of the averaged $\overline{Nu}_h$ and $\overline{Nu}_c$ numbers and the corresponding Fourier spectra obtained for the values of $\delta = 0.4$, $Ra = 6.25 \times 10^6$.

the previous section by $Ra_L = Ra \times (L/a)^3$.

In practice, three configurations with the geometry characteristics given in Table 1 were analyzed for the range of $Ra_L \in [10^6 \div 10^9]$. The $Nu_L - Ra_L$ functionalities deduced from the corresponding experimental data are presented in the fourth column of Table 1.

A comparison of the numerically obtained results with data based on the experimentally deduced correlations is presented in Fig. 2. It can be seen that the numerically obtained Nu_L values are somewhat lower than the corresponding experimental values. The apparent reason for this discrepancy could be the uncertainty related to the estimation of the radiative losses for air in experiments, which (according to the authors) were of the order of 70% [28]. Remarkably, the discrepancy between the numerical and the experimental results increases with increasing Ra_L values (i.e., with the temperature difference, as Ra_L is proportional to the temperature difference for the same working liquid), which further implicates the uncertainty related to the estimation of the radiative losses as a major factor for the observed discrepancy. Nonetheless, both experimental and numerical results exhibit a power law $Nu_L - Ra_L$ functionality in agreement with the boundary layer theory. Additionally, the same trend of a decreasing Nu_L value with an increasing radius of the sphere is observed for both numerically and experimentally obtained results. To further prove the correct implementation of the utilized numerical solver, an extensive verification study focussing on the configurations directly related to the current research is presented in the next section.

4. Verification study

The method used in the current study was verified by simulating the natural convection flow developing around a hot cylinder placed horizontally along the horizontal centerline of a cold cubic cavity. The obtained flow characteristics were compared with the corresponding results reported in Ref. [18]. Note that the results summarized in this paper appear in our previous study [21] and are repeated here for the sake of completeness of the verification study. An additional metric that was used for the verification purposes was the global Nusselt number $\overline{Nu}_G$ which provides a measure of the overall heat flux through the boundaries of the cubic enclosure and is defined as:

$$\overline{Nu}_G = \frac{1}{N}\sum_{i=1}^{N}\frac{\overline{\partial\theta}}{\partial n}, \tag{5}$$

where $N = 4$ is the total number of faces of the cubic cavity that are not thermally insulated and $\frac{\overline{\partial\theta}}{\partial n}$ is the value of the temperature gradient averaged over the i^{th} face of the cavity. The results were obtained for the range of $Ra = \in [10^4 \div 10^6]$ and $R/L = \in [0.1 \div 0.4]$. A detailed comparison between the Nu and Nu_G numbers obtained for the entire range of Ra and R/L values is presented in Table 2. It can be seen that

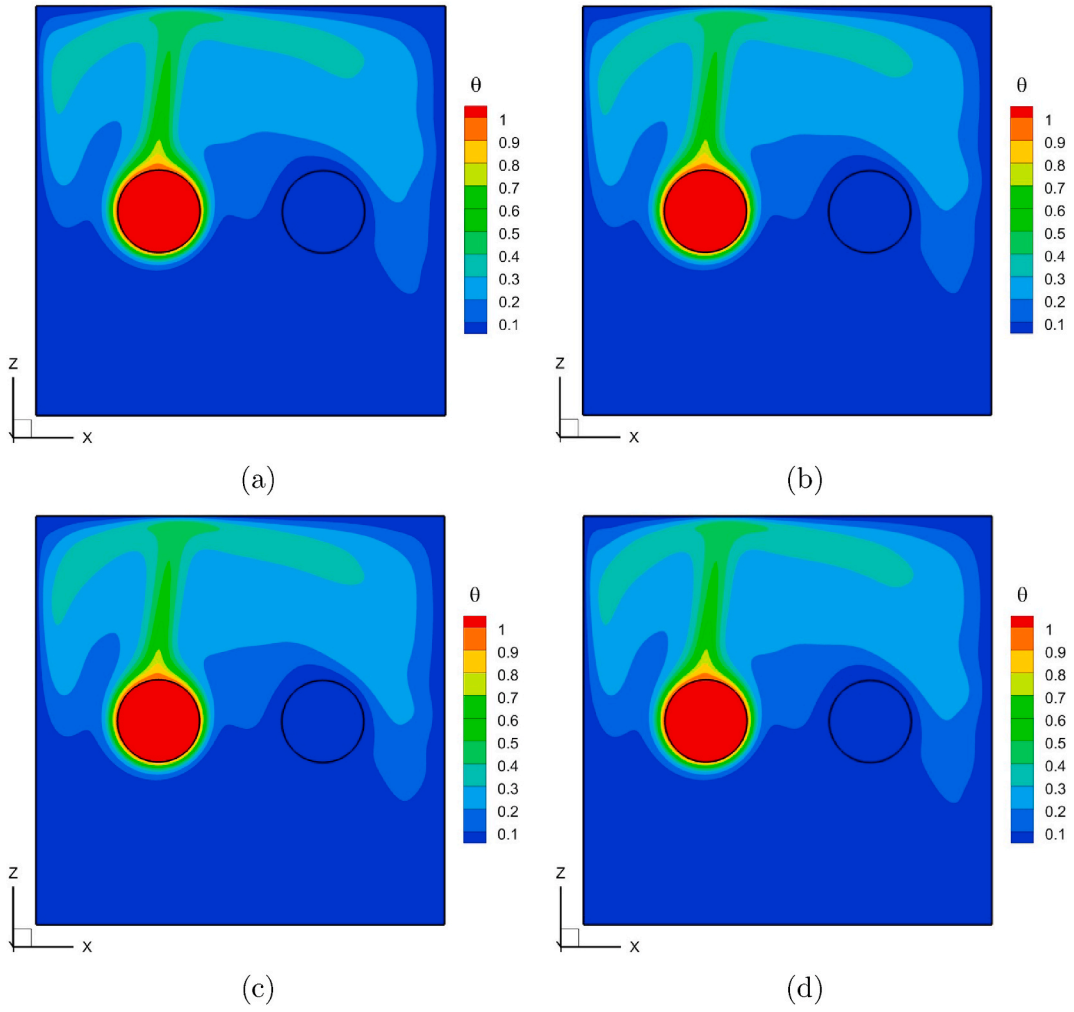

Fig. 5. Temperature distribution in the midplane $(X-Z)$ of the cubical enclosure obtained for 4 representative time instances of the $\overline{Nu_h}$ time evolution as shown in Fig. 4: (a) maximal value of $\overline{Nu_h}$ (P1); (b) intermediate value of $\overline{Nu_h}$ (P2); (c) minimal value of $\overline{Nu_h}$ (P3); and (d) intermediate value of $\overline{Nu_h}$ (P4). The data was obtained for values of $\delta = 0.4$, $Ra = 6.25 \times 10^6$.

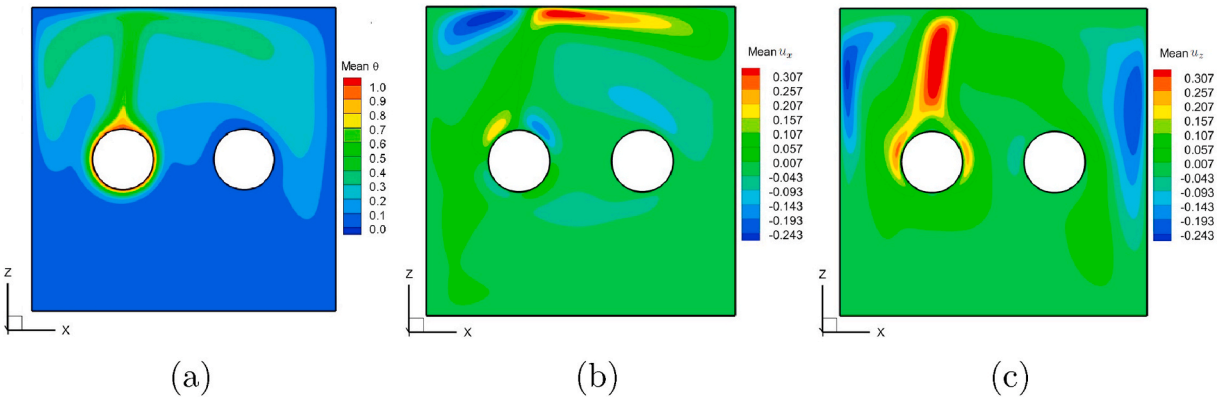

Fig. 6. Distribution of the mean flow characteristics obtained in the midplane $(X-Z)$ for: (a) mean temperature θ; (b) mean u_x velocity component; and (c) mean u_z velocity component. $\delta = 0.4$, $Ra = 6.25 \times 10^5$. The results were obtained on a 200^3 structured uniform grid.

acceptable agreement exists between the currently obtained values of Nu and Nu_G numbers and the corresponding data reported in Refs. [18], while the maximal deviation is observed for $R/L = 0.4$ and does not exceed 3%.

We also compared the flow characteristics in terms of the iso-contours of temperature and the iso-surfaces of the λ_2 criterion, which correlates with the vortical structure of the flow. The results were obtained for $Ra = 10^6$ and for R/L values lying in the range of $R/L \in [0.1 \div 0.4]$ as shown in Fig. 3. It can clearly be seen that the distributions of the flow characteristics obtained in the verification study are in acceptable qualitative agreement with those presented in Ref. [18] for the entire range of parameters, with exception of $R/L = 0.4$. It should be noted

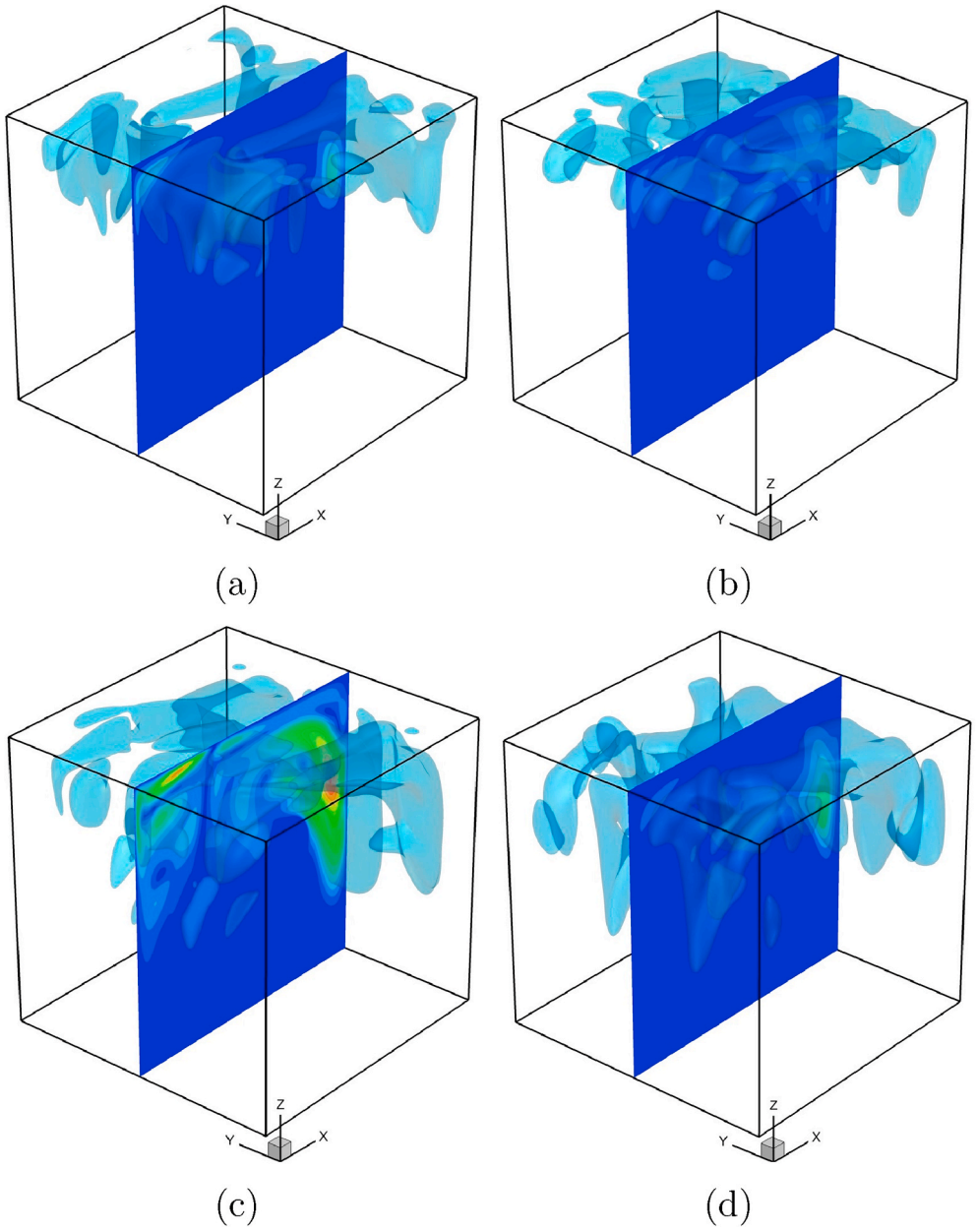

Fig. 7. Isosurfaces of oscillation amplitudes obtained for: (a) temperature, θ; (b) u_x velocity component; (c) u_y velocity component; and (d) u_z velocity component. The isosurfaces confine the regions characterized by at least 25% of the absolute maximum value. Colors correspond to relative intensity of the oscillations. $\delta = 0.4$, $Ra = 6.25 \times 10^6$.

here that all the currently performed simulations yielded steady state flows while the reference study [18] reported unsteady flows for $Ra = 10^6$ and $R/L = 0.3$ and $R/L = 0.4$ values. For this reason, the values for these unsteady flows reported in Ref. [18], and presented here in Table 2, have been time averaged. For the value $R/L = 0.3$, the deviations between the currently obtained results and the reference results [18] are insignificant and can be simply explained by the differences in the implementation of the two methods. Nonetheless, the differences observed in the spatial distribution of the λ_2 criterion for $Ra = 10^6$ and $R/L = 0.4$ appear to indicate that the two solutions belong to different branches simultaneously existing for the same operating conditions. This type of finding is typical of non-linear systems and requires an in-depth investigation which is beyond the scope of the present study. The reliability of our currently described method was corroborated by an extensive grid independence study, which is described in the next section for all the obtained results.

5. Results and discussion

To demonstrate the factors that characterize different scenarios of the development of flow instability in highly separated confined natural convection flows the characteristics of slightly supercritical flow are now analyzed for the 3 different combinations of distance δ and Ra numbers, namely, for $\delta = 0.4, 0.5$ and $Ra = 6.25 \times 10^6$ and for $\delta = 0.6$ and $Ra = 1.4 \times 10^6$. The instability characteristics are investigated in terms of the time evolution of the $\overline{Nu}$ values, the distribution of the instantaneous temperature fields θ, and the distribution of the temperature and all the velocity component fields averaged over a single oscillating period.[1] Further, the spatial distribution of the isosurfaces of

[1] Both distributions are taken at the vertical mid cross section of the cubic enclosure.

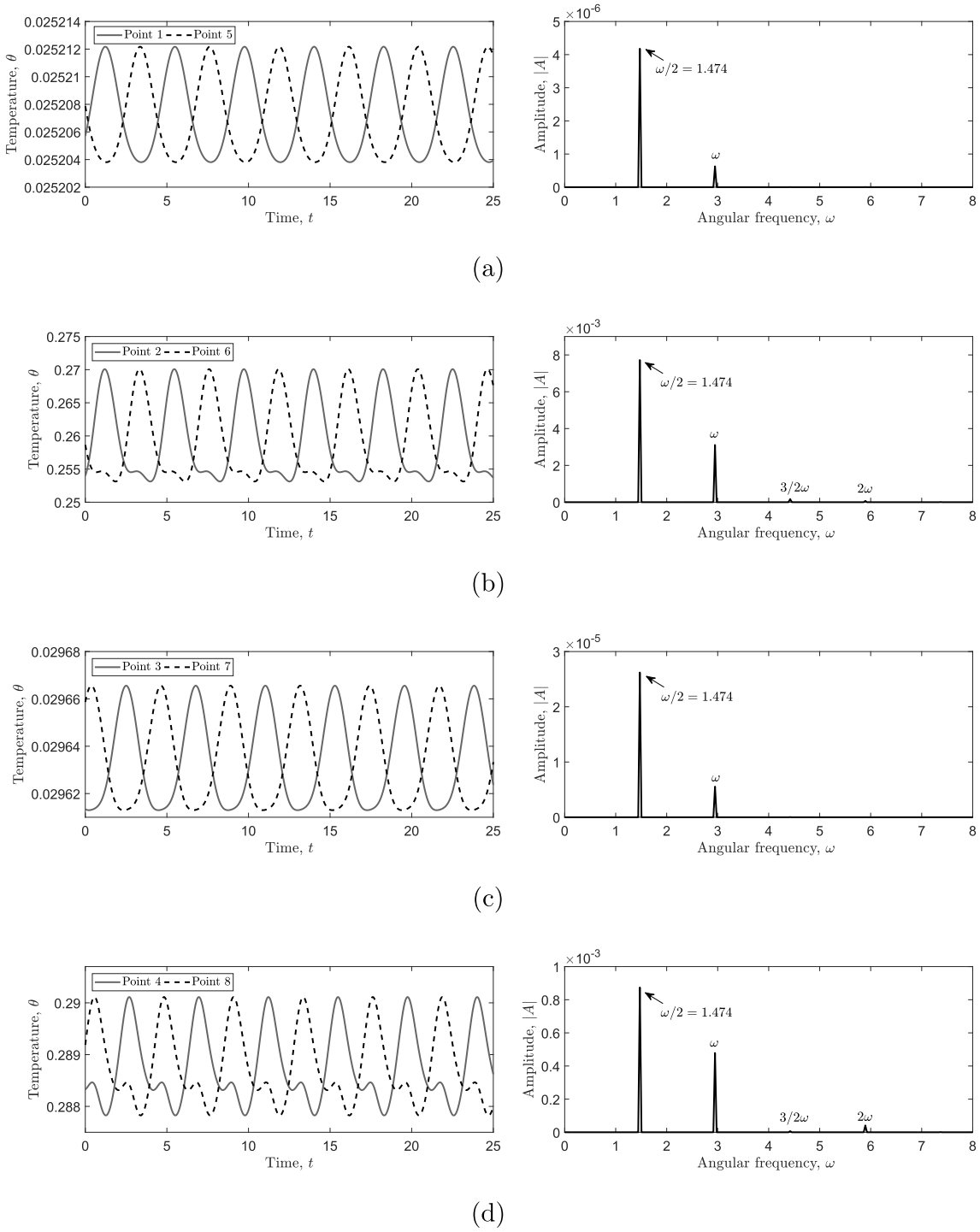

Fig. 8. Time evolutions and Fourier spectra monitored at four pairs of points symmetrically positioned relative to the $(X-Z)$ midplane for $\delta = 0.4$, $Ra = 6.25 \times 10^6$: (a) P1 and P5; (b) P2 and P6; (c) P3 and P7; (d) P4 and P8. The results were obtained on a 200^3 structured uniform grid.

the oscillation amplitudes of all the flow fields and the evolution of the temperature values are monitored at 8 representative control points – designated P1 to P8 – as detailed in Table 3. For all the configurations, zero values for the pressure, for the temperature of the interior of the cavity and both cylinders as well as for all the velocity components were set as initial conditions, whereas slightly supercritical flow was recognized by taking the steady state flow characteristics obtained for a certain subcritical value of *Ra* as the initial condition and gradually increasing the value of *Ra* (each time by 5%) until the steady-unsteady transition took place. No-slip boundary conditions were set at all the cavity boundaries and on the surfaces of the immersed cylinders. The convergence to steady state was assumed when the maximal value of the L_∞ norm calculated for the relative difference between all the flow fields obtained in two consecutive time steps was less than $L_\infty \leq 10^{-5}$. All the Fourier frequency spectra obtained for the *Nu* values averaged over the surfaces and temperature values measured at the 8 control points are based on data acquired for 100 oscillating periods.

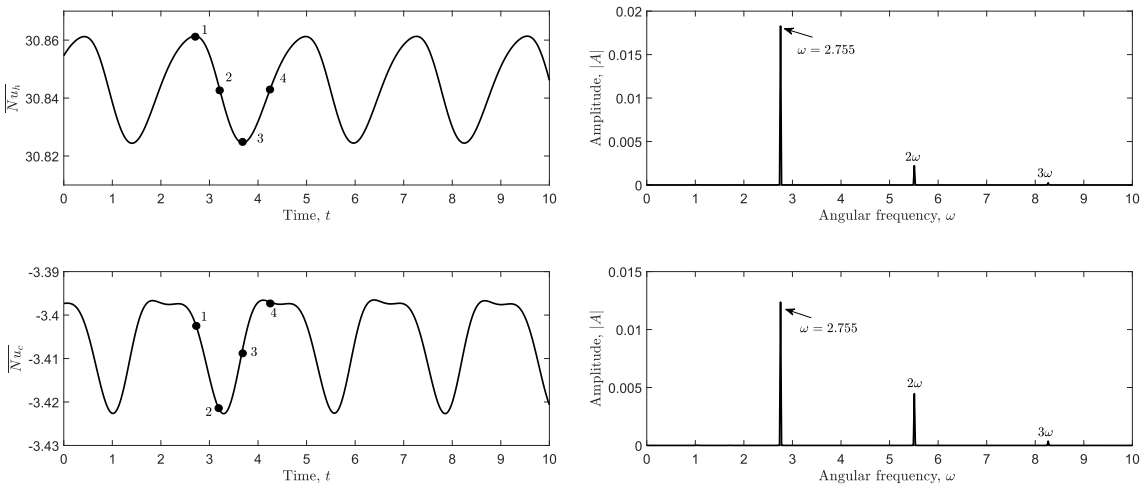

Fig. 9. Time evolution of the averaged $\overline{Nu}_h$ and $\overline{Nu}_c$ numbers and the corresponding Fourier spectra obtained for the values $\delta = 0.5$, $Ra = 6.25 \times 10^6$.

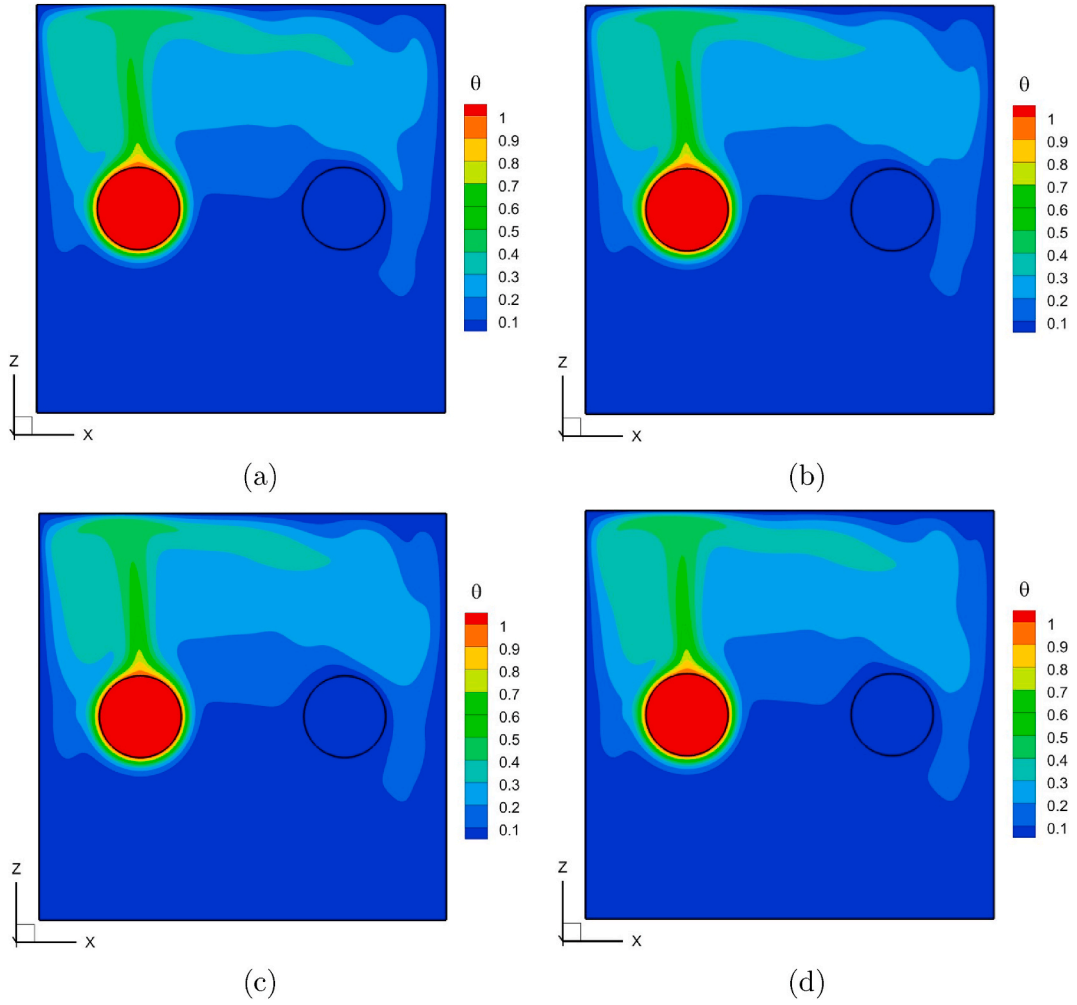

Fig. 10. Temperature distribution in the midplane $(X-Z)$ of the cubical enclosure obtained for 4 representative time instances of the $\overline{Nu}_h$ time evolution as shown in Fig. 9: (a) maximal value of $\overline{Nu}_h$ (P1); (b) intermediate value of $\overline{Nu}_h$ (P2); (c) minimal value of $\overline{Nu}_h$ (P3); and (d) intermediate value of $\overline{Nu}_h$ (P4). The data was obtained for the values of $\delta = 0.5$, $Ra = 6.25 \times 10^6$.

5.1. Grid independence study

To prove the grid independence of the obtained results, the simulations were performed on 200^3 and 300^3 grids. The results obtained on two grids for slightly supercritical flow regimes were compared in terms of maximal and minimal values of the Nusselt numbers $\overline{Nu}_c$ and $\overline{Nu}_h$, averaged over the surfaces of the cold and hot cylinders, respectively. The comparison is detailed in Table 4. It can be seen that for the entire

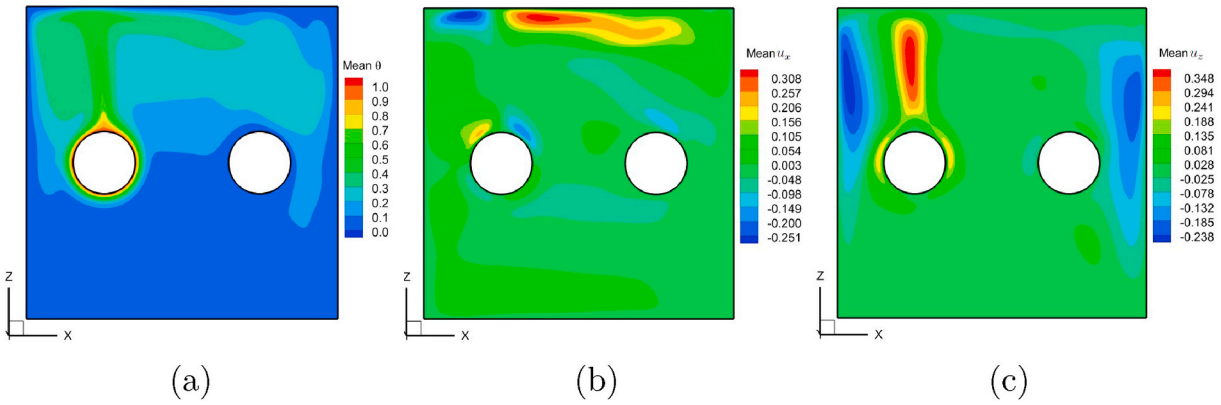

Fig. 11. Distribution of the mean flow characteristics obtained in the midplane $(X-Z)$ for: (a) mean temperature θ; (b) mean u_x velocity component; and (c) mean u_z velocity component. $\delta = 0.5$, $Ra = 6.25 \times 10^6$. The results were obtained on a 200^3 structured uniform grid.

range of δ and Ra values the maximal deviation between the averaged Nu values obtained on the two grids does not exceed 0.6%, which proves the grid independence of the obtained results.

We now compare the maximal and minimal values of the temperature acquired pointwise on the two grids at points P4, P2, and P1 (see Table 5). Again, the results obtained on the two grids are in excellent agreement, while the maximal deviation between the corresponding values does not exceed 0.7%. It should be noted that the computational time increases rapidly from the 200^3 to the 300^3 grid. In particular, it took about 4 and 12 days run the simulations on the 200^3 and 300^3 grids, respectively, to reach a periodic regime of the flow. Further, it took about 3 weeks to acquire a long-time periodic statistics (100 periods) when running the simulations on the 200^3grid, while it is expected to take 9 weeks on the 300^3 grid. Given the excellent agreement between the results obtained on the 200^3 and 300^3 grids for flows that had already reached periodic regimes, grid independence of the results obtained on the 200^3 grid was proved, allowing us to perform all further simulations of long-term periodic flows on a 200^3 grid.

5.2. *Configuration characterized by the value of $\delta = 0.4$*

The time evolution of the Nusselt numbers $\overline{Nu_h}$ and $\overline{Nu_c}$ averaged over the surfaces of the hot and cold cylinders, respectively, with the corresponding Fourier spectra are shown in Fig. 4. As expected for the slightly supercritical regime, the signals oscillate with a very small amplitude (less than 0.5% of the mean value) and are governed by a single oscillating harmonic $\omega = 2.932$. It is remarkable that the mean of $\overline{Nu_c}$ is about an order of magnitude less than the value of $\overline{Nu_h}$, constituting clear evidence of the domination of the heat flux leaving the hot cylinder compared to that absorbed by the cold cylinder. This observation may be attributed to the fact that four of the cavity walls are held at the cold temperature T_h. We note in passing that the value of $\overline{Nu_h}$ obtained in our previous study [21] for vertical tandem cold and hot cylinders and the same value of $\delta = 0.4$ was also higher than the $\overline{Nu_c}$ value by about an order of magnitude. Therefore, despite entirely different flow regimes, the spatial orientation of the hot and cold cylinders does not seem to have a strong effect on the ratio between the heat emanating from the hot cylinder and that absorbed by the cold one when both cylinders are placed within a cold cubic container.

The temperature distribution in the mid cross-section of the cubical enclosure corresponding to 4 representative time instances over a single period of $\overline{Nu_h}$ and $\overline{Nu_c}$ values (i.e., points 1,2,3 and 4 in Fig. 4-a and 4-c) is shown in Fig. 5. When the hot plume rising from the surface of the hot cylinder meets the horizontal top boundary, it separates into two oppositely directed streams, redirecting warm air flows towards the vertical left and right walls. It is remarkable that in this configuration the cold cylinder acts as a thermal sink, attracting the hot air and pushing it down the horizontal centerline passing through the centers of the hot and cold cylinders. Note also the tilt of the thermal plume towards the right side of the cavity throughout the oscillation period; this tilt to the right is the result of the effect of the cold cylinder and of the unequal distances from the center of the hot cylinder to the left and right vertical walls of the cavity. It is also remarkable that, despite the supercritical flow regime, the thermal plume is almost stationary, and that slight temporary variations in the temperature distribution are localized in the region lying between the surface of the cold cylinder and the adjacent vertical wall of the cavity.

The plume tilt observed in Fig. 5 for the temperature distribution of time instances corresponding to the maximal and minimal values of $\overline{Nu_h}$ and $\overline{Nu_c}$ is reflected in the distribution of the mean temperature θ and of the u_x and u_y fields demonstrated in Fig. 6. Note that for this setup the mean value of the u_y velocity component is equal to zero and is therefore not shown in Fig. 6. Note also the close positive and negative values of the u_x velocity component closest to the top boundary of the cavity (see Fig. 6-(b)), which constitutes clear evidence for the flow separation in the region where the rising thermal plume approaches the top wall.

In slightly supercritical oscillatory regimes, the spatial structure of the absolute value of the leading eigenvector of each flow field can be obtained by constructing the spatial distribution of the corresponding oscillating amplitudes acquired over a single oscillating period [21,29,30]. The amplitude isosurfaces confining the regions characterized by at least 25% of the absolute maximum value are shown in Fig. 7 for the temperature and all the velocity components. It is noteworthy that for all the fields the regions characterized by the highest values of the oscillating amplitudes are localized in the upper part of the cavity, which is a result of flow blocking effects of the cavity top wall resulting in separating the hot plume rising from the hot cylinder and, eventually, leading to a sharp change of the flow direction. Note also the symmetric structure of the isosurfaces relative to the $X-Z$ midplane. This observation leads us to conclude that over a single period the flow oscillates with the same amplitudes in both parts of the cavity separated by the $X-Z$ midplane.

To address the question regarding the spatio-temporal characteristics of the observed oscillatory instability, we now analyze the temperature signals acquired at the 8 control points whose coordinates are given in Table 3. In particular, we focus on the 4 pairs of points evenly distributed spanwise in the vicinity of the cavity edges and placed on opposite sides relative to the $X-Z$ midplane. The acquired signals with the corresponding Fourier spectra are shown in Fig. 8. Note that, as expected for the slightly supercritical regime dominated by a leading eigenmode, all the signals oscillate with a single angular frequency $\omega = 1.474$ and its multipliers appearing as result of the flow non-linearity. Two important observations are that the frequency value is exactly half of that

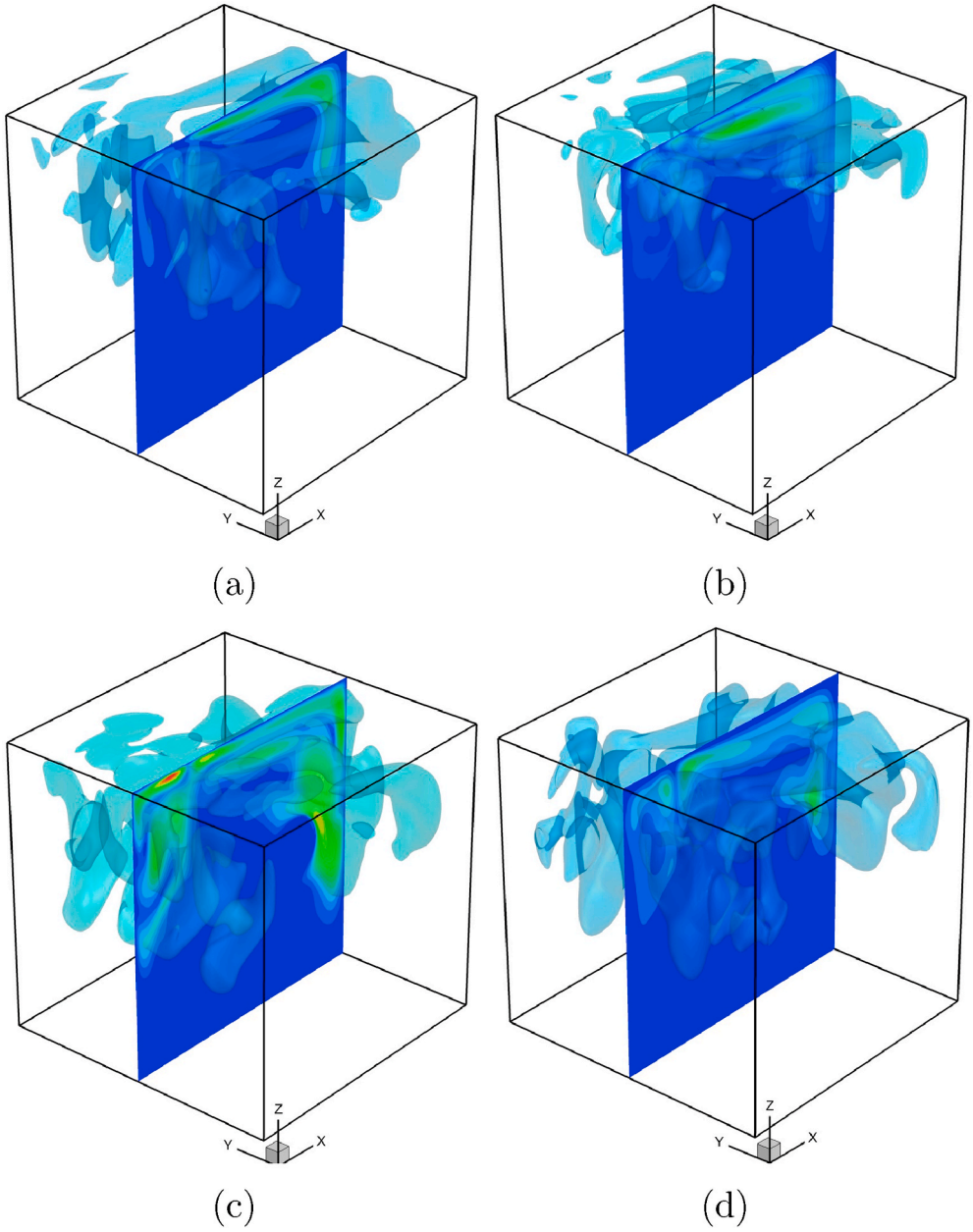

Fig. 12. Isosurfaces of oscillation amplitudes obtained for: (a) temperature, θ; (b) u_x velocity component; (c) u_y velocity component; and (d) u_z velocity component. The isosurfaces confine the regions characterized by at least 25% of the absolute maximum value. Colors correspond to the relative intensity of the oscillations. $\delta = 0.5$, $Ra = 6.25 \times 10^6$.

previously determined for $\overline{Nu_c}$ and $\overline{Nu_h}$ and that the time signals acquired at each pair of points are biased by half a period. Thus, it can be concluded that the flow undergoes bifurcation characterized by spatio-temporal symmetry H half a period apart, preserving the Y_2 symmetry group [31] and formally expressed as:

$$H\boldsymbol{u}(\boldsymbol{X}',t) = K_{Y'}\boldsymbol{u}(\boldsymbol{X},t+T/2) = (u_{X'},-u_{Y'},u_{Z'})(X',-Y',Z',t+T/2), \quad (6)$$

with H-symmetric base flow $H\overline{\boldsymbol{u}}(\boldsymbol{X}') = K_{Y'}\overline{\boldsymbol{u}}(\boldsymbol{X}')$, where $K_{Y'}$ is the spatial reflection, i.e., $Y' \rightarrow -Y'$, $u_{Y'} \rightarrow -u_{Y'}$ and T is the period of the perturbed flow oscillations. Note that exactly the same scenario was revealed with respect to the bifurcated shear flow inside a diagonally lid driven cavity [32], and also with respect to the bifurcated natural convection flow developing within a cubic enclosure in the presence of a vertical tandem of hot and cold cylinders[2] [21].

5.3. Configuration characterized by the value of $\delta = 0.5$

To further investigate the effect of the distance between the cylinders and the vertical walls of the cubic enclosure on the characteristics of the observed instability, the slightly supercritical flow developing for the $\delta = 0.5$ and $Ra = 6.25 \times 10^6$ scenario is now considered. Fig. 9 presents the time evolution of the $\overline{Nu_h}$ and $\overline{Nu_c}$ numbers averaged over the surfaces of the hot and cold cylinders, respectively, with the corresponding frequency spectra. As expected, the signals monitored for both $\overline{Nu}$ values are governed by a single oscillating harmonic and its multipliers whose

[2] The result was obtained for the value of $\delta = 0.5$.

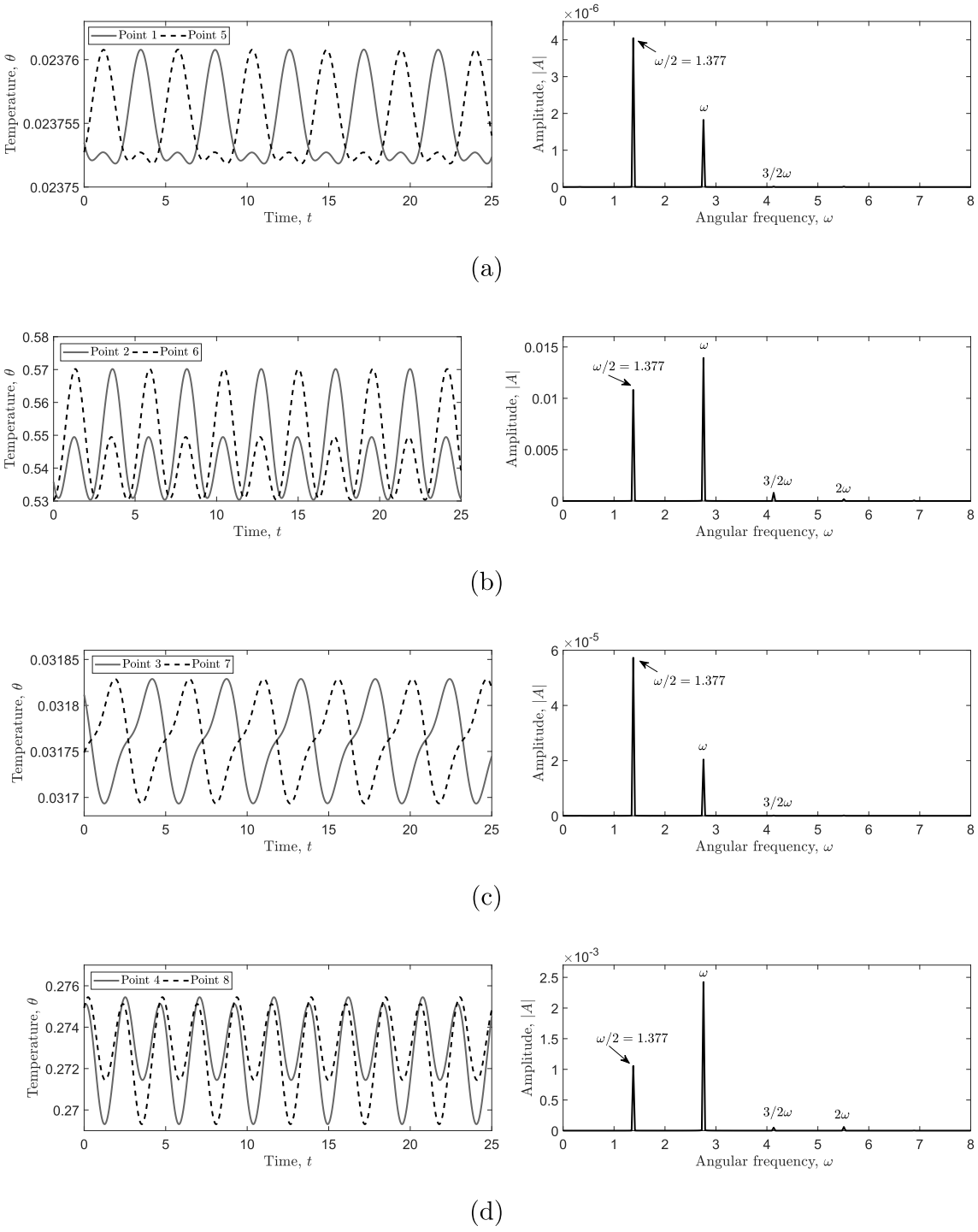

Fig. 13. Time evolutions and Fourier spectra monitored at four pairs of points symmetrically positioned relative to the $(X-Z)$ midplane for $\delta = 0.5$, $Ra = 6.25 \times 10^6$: (a) P1 and P5; (b) P2 and P6; (c) P3 and P7; (d) P4 and P8. The results were obtained on a 200^3 structured uniform grid.

value $\omega = 2.755$ is close to that obtained for the configuration described in the previous section. Note that the slightly supercritical flow is observed at the same value of the Ra number. Note also that the $\overline{Nu_h}$ to $\overline{Nu_c}$ ratio is about the same as that observed for the $\delta = 0.4$ with a slight decrease, which could be a consequence of the growing impact of the flow-blocking effects exerted on the flow by the vertical boundary of the container adjacent to the surface of the hot cylinder.

Despite the similarity in the time signals of $\overline{Nu_c}$ and $\overline{Nu_h}$ obtained for the present and the previous configurations, the flow regimes developing in the two configurations are quite different. In fact, both instantaneous temperature distributions in the mid cross-section of the cubical enclosure (see Fig. 10) and the distributions of the mean flow characteristics (see Fig. 11) obtained in the midplane $(X-Z)$ of the cubical enclosure are characterized by the waviness observed for all the flow characteristics in the region lying between the hot and cold cylinders close to the top boundary of the cubic enclosure. Additionally, temporal deviation of the temperature field over the oscillation period can be recognized in much wider region compared to the previous configuration. Note also the considerably wider region occupied by the positive value of the u_x component compared to that occupied by the

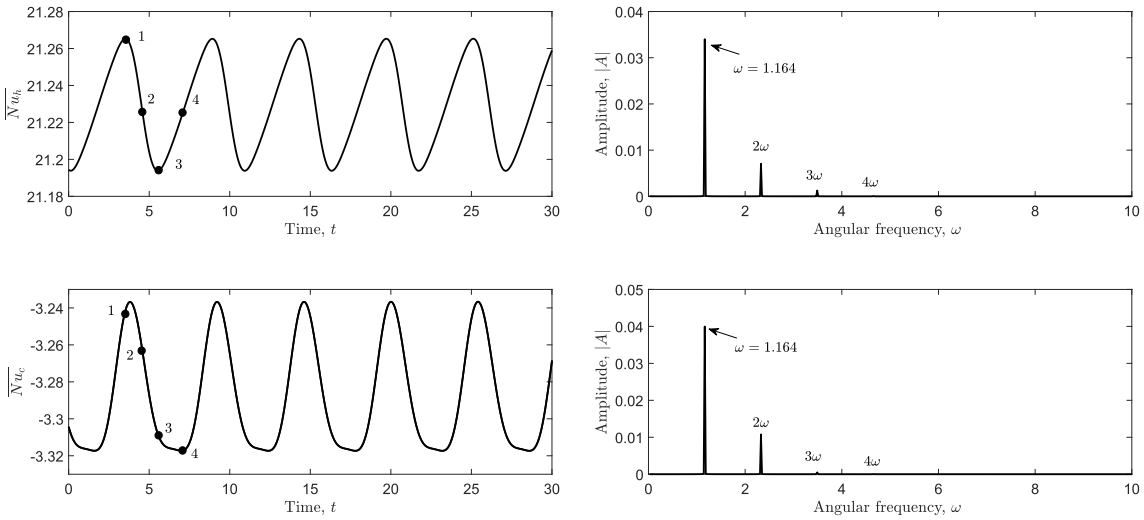

Fig. 14. Time evolution of the averaged $\overline{Nu}_h$ and $\overline{Nu}_c$ numbers and the corresponding Fourier spectra obtained for the values of $\delta = 0.6$, $Ra = 1.4 \times 10^6$.

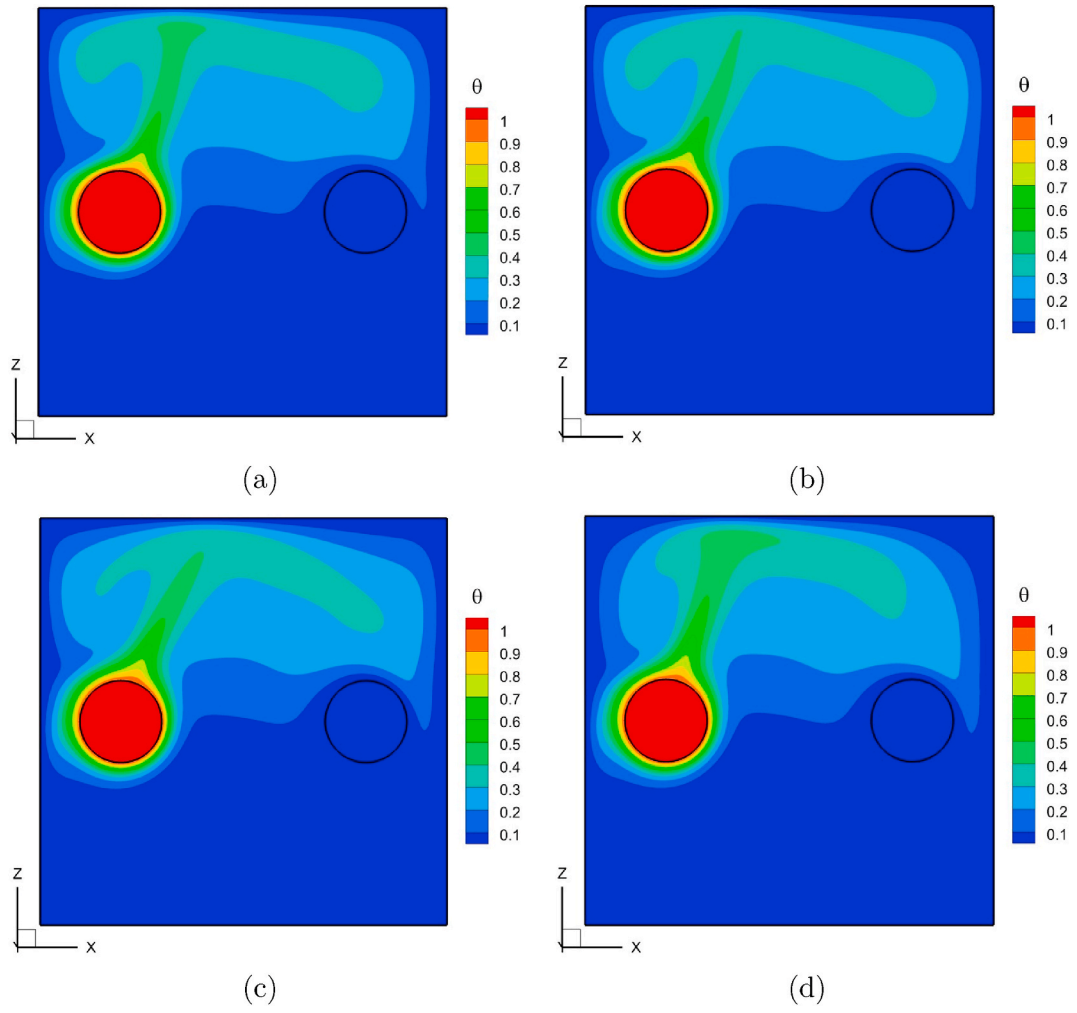

Fig. 15. Temperature distribution in the midplane $(X-Z)$ of the cubical enclosure obtained for 4 representative time instances of the $\overline{Nu}_h$time evolution as shown in Fig. 14: (a) maximal value of $\overline{Nu}_h$ (P1); (b) intermediate value of $\overline{Nu}_h$ (P2); (c) minimal value of $\overline{Nu}_h$ (P3); and (d) intermediate value of $\overline{Nu}_h$ (P4). The data was obtained for the values of $\delta = 0.6$, $Ra = 1.4 \times 10^6$.

negative one. Both observations clearly indicate an increasing non-uniformity in the separation of the thermal plume (compared to the previous configuration) once the latter reaches the top of the cavity, while the waviness observed is apparently a consequence of oscillations inherent to all the flow fields in the region hosting the right more energetic branch of the hot plume.

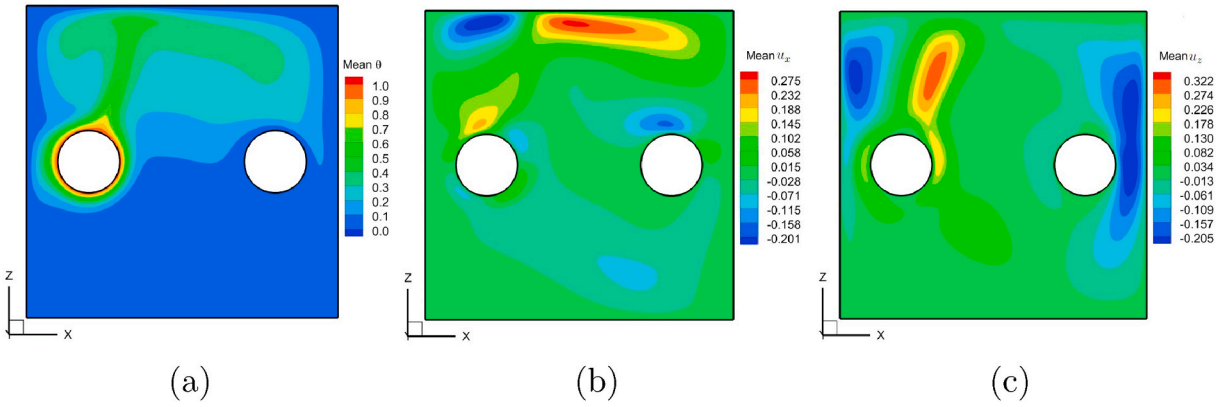

Fig. 16. Distribution of the mean flow characteristics obtained in the midplane $(X-Z)$ for: (a) mean temperature θ; (b) mean u_x velocity component; and (c) mean u_z velocity component. $\delta = 0.6$, $Ra = 1.4 \times 10^6$. The results were obtained on a 200^3 structured uniform grid.

The assumption as to the origin of the observed waviness is further confirmed by examining the isosurfaces of the oscillation amplitudes shown in Fig. 12. In fact, the vicinity of the right branch of the hot plume is characterized by high amplitude values for all the flow characteristics, indicating the most unstable region of the observed oscillatory flow. It is also noteworthy that, similarly to the configuration characterized by the value of $\delta = 0.4$, the spatial distribution of the isosurfaces of the oscillating amplitudes is symmetric relative to the midplane $(X - Z)$, which means that the flow oscillates with the same values of the amplitude in both parts of the cubic enclosure.

We now perform the same analysis as for the previous configuration, namely, monitoring the time evolutions of the temperature field at 4 pairs of control points, as detailed in Table 3. The analysis provides deeper insights into the spatio-temporal characteristics of the observed instability. The time histories for each pair of points with the corresponding Fourier spectra are shown in Fig. 13. An examination of the time evolution of temperature shows that, similarly to the previous configurations, the time signals are biased by half a period (up to a tiny offset that is apparently a consequence of the non-negligible inertia effects of the flow). The character of the observed bifurcation thus belongs to the same symmetry group characterized by Eq. (6). The slightly supercritical flow is characterized by the different flow dynamics governing the natural convection flow in the lower and upper halves of the cubic enclosure, as follows: while the lower half of the enclosure is characterized by an almost steady flow regime ($O(A)\tilde{}10^{-6}$), the temperature is dominated by a mode characterized by half the angular frequency compared to that observed for the $\overline{Nu}_h$ and $\overline{Nu}_c$ time evolutions (see Fig. 9 and Fig. 13(a) and (c)). Further, the upper half of the enclosure, characterized by a more pronounced bifurcated flow ($O(A)\tilde{}10^{-3}$), is governed by the mode having the same frequency as that governing the $\overline{Nu}_h$ and $\overline{Nu}_c$ time signals (see Fig. 9 and Fig. 13(b) and (d)).

5.4. Configuration characterized by the value of $\delta = 0.6$

To further investigate the impact of the distance between the cylinder centers and the vertical boundaries of the cubic enclosure on the instability mechanisms, we performed numerical simulations of the flow developing in the configuration characterized by the value of $\delta = 0.6$. Following the methodology applied for the previous configurations, we first determine the value of $Ra = 1.4 \times 10^6$, corresponding to a slightly supercritical flow regime. Note that, despite expectations of an increasing damping effect of the vertical walls of the cavity, which should have reduced the momentum of the convective flow, this Ra value is significantly lower than that obtained for the previous two configurations. This fact indicates that the distance between the cylinders constitutes the characteristic scale determining the instability characteristics typical of a tandem of horizontally aligned hot and cold cylinders. We now perform the analysis of the time evolution of the $\overline{Nu}_h$ and $\overline{Nu}_c$ values averaged over the surfaces of hot and cold cylinders, respectively, as presented in Fig. 14. It can be seen that the value of the angular frequency $\omega = 1.164$ of the leading mode is less than half the corresponding values obtained for the configurations characterized by the values of $\delta = 0.4$ and $\delta = 0.5$, indicating a different instability mechanism. This finding can be attributed to the increasing impact of the vertical walls, which stabilize the oscillatory flow by decreasing the angular frequency of the oscillations.

The increasing impact of the vertical walls is clearly evident upon examination of the temperature distribution in the midplane $(X-Z)$ of the cubical enclosure obtained over the single oscillation period of $\overline{Nu}_h$ (see Fig. 15). It can be seen that for all the time instances the thermal plume rising from the hot cylinder is biased towards the cold cylinder, playing the role of a thermal sink. As an interesting observation, we note that in contrast to the two previous configurations the maximal deviation in the temperature distribution is exhibited in the central region of the thermal plume, where we can expect the existence of the maximal oscillation amplitudes of all the flow fields.

The bias of the rising thermal plume towards the surface of the cold cylinder observed for the temperature distribution is also evident for the u_x and u_z velocity components, as follows from the distribution of mean flow characteristics shown in Fig. 16. In fact, the absolute values of the maxima of both velocity components are higher than the corresponding minima values by at least 35%, which is a significantly larger difference than that found with the other two configurations. Thus, it can be concluded that after the thermal plume separates in the vicinity of the top boundary the average flow rate redirected to the right is significantly higher than that redirected to the left; this is a direct consequence of the increasing flow-blocking effects of the vertical walls suppressing the momentum of the flow.

As has already been mentioned, the central region of the thermal plume is characterized by the maximal deviation in the temperature distribution; this raises the possibility of the existence of the maximal oscillation amplitudes of all the flow fields in this region, as confirmed by Fig. 17. In fact, for the θ, u_x and u_z fields, the isosurfaces of the maximal oscillation amplitudes are concentrated within the region hosting the rising thermal plume. At the same time, the amplitude isosurfaces corresponding to the u_y velocity component are distributed over the entire upper part of the cavity, while the value of the oscillating amplitude over the entire $X - Z$ midplane is equal to zero. It is also noteworthy that, similarly to the two other configurations, the distributions of oscillation amplitudes shown in Fig. 17 are symmetric relative to the $X - Z$ midplane.

We now repeat the analysis performed for the configurations characterized by the values of $\delta = 0.4$ and $\delta = 0.5$ and present the time

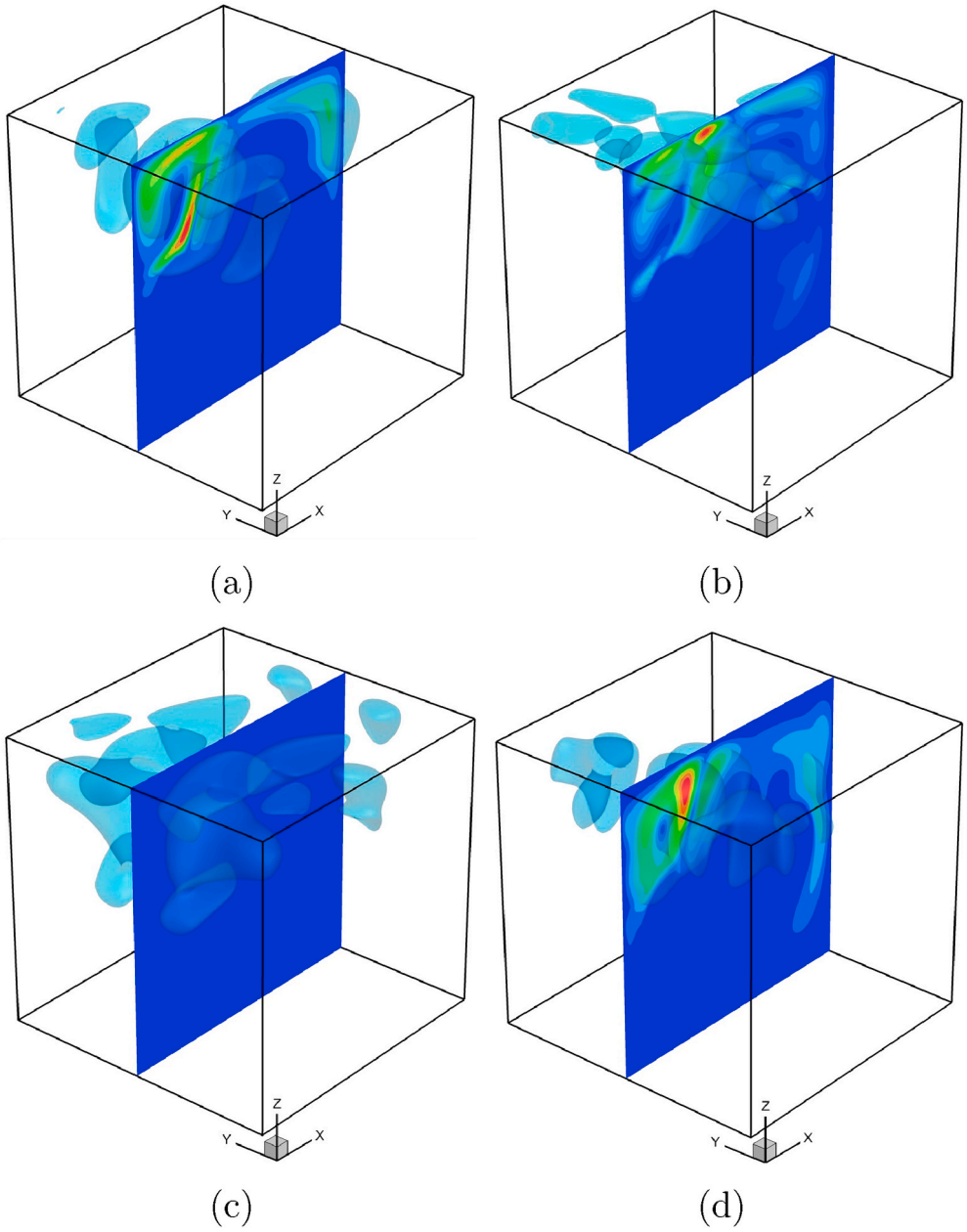

Fig. 17. Isosurfaces of oscillation amplitudes obtained for: (a) temperature, θ; (b) u_x velocity component; (c) u_y velocity component; (d) u_z velocity component. The isosurfaces confine the regions characterized by at least 25% of the absolute maximum value. Colors correspond to the relative intensity of the oscillations. $\delta = 0.6$, $Ra = 1.4 \times 10^6$.

evolution with the corresponding Fourier spectra of temperatures monitored at 4 pairs of control points (see Table 3) symmetrically placed relative to the $X - Z$ midplane (see Fig. 18). It can be seen that both signals acquired at each pair of points completely coincide with each other, while the bifurcation observed is characterized by spatio-temporal symmetry H preserving the Y_2 symmetry group. Note that the same symmetry group was also preserved for the vertical tandem of hot and cold cylinders characterized by the value of $\delta = 0.6$ [21], which could be related to an increasing stabilizing effect imposed by the boundaries of the cubic enclosure.

6. Summary and conclusions

Heat transfer patterns and flow surrounding immersed objects were extensively investigated in this paper. The immersed objects were horizontally aligned cylinders maintained at a constant temperature (one hot and the other cold), and the container was a cubic cavity with all walls, except for the adiabatic front and back walls, being held at a constant cold temperature. In particular, instability phenomena in the developed supercritical flow (convectional in nature) were studied by means of numerical simulations. The horizontal orientation of the immersed objects constitutes the incremental, but substantial, difference between this work and our preceding studies on the same thermo-fluid dynamical interactions. The geometrical configurations, methodologies and flow regimes were the same as those in our previous work with the aim to afford the possibility of constructing a comprehensive corpus of in-depth research of highly similar scenarios. Once again, the separation distance between the two cylinders was found to be highly influential. The values of $\delta = 0.4, 0.5$ and 0.6 corresponding to Rayleigh numbers of $Ra = 6.25 \times 10^6$ and $Ra = 1.4 \times 10^6$, respectively, were found to yield the transition between steady and unsteady flow. The transition to unsteadiness was determined by gradually increasing the

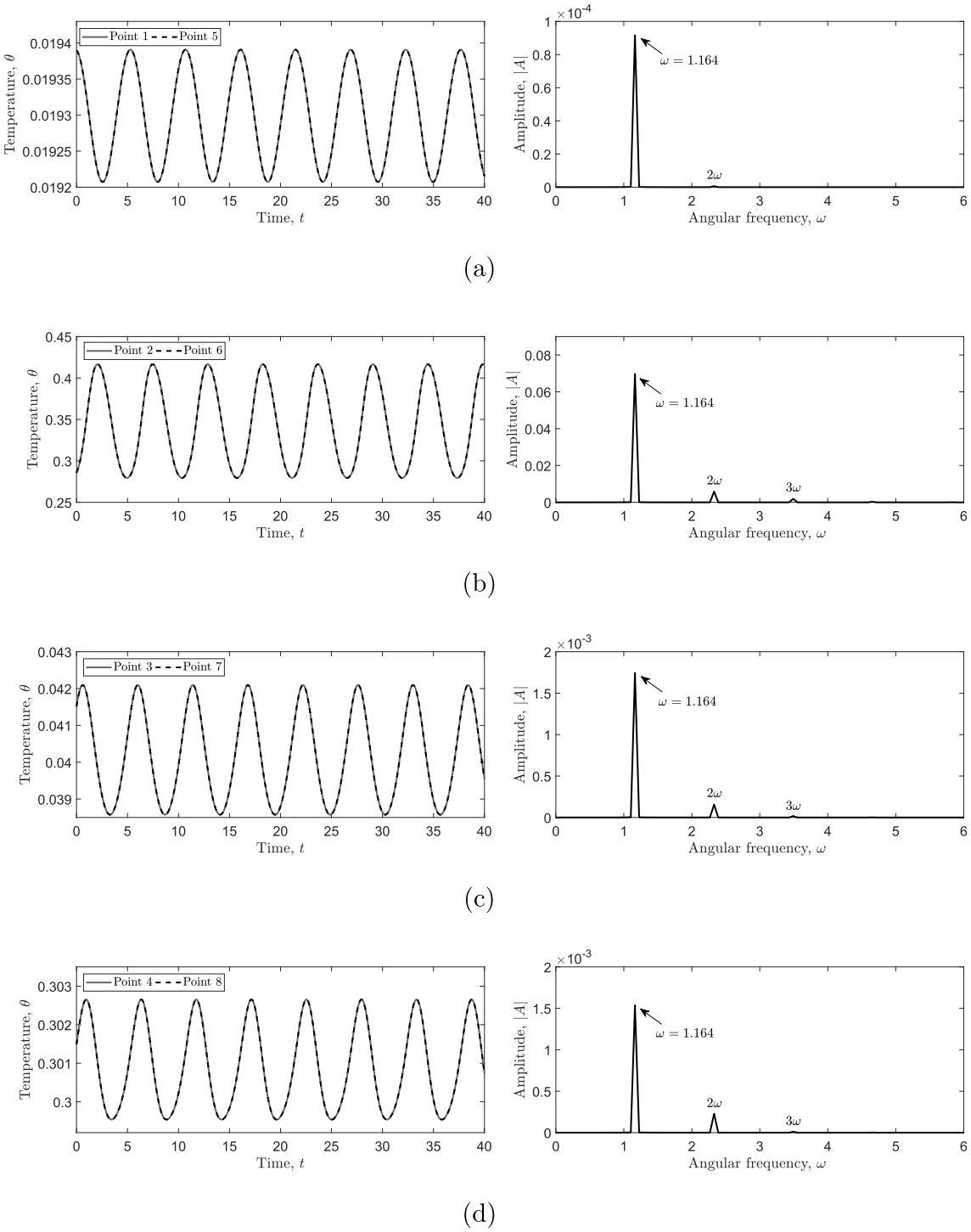

Fig. 18. Time evolutions and Fourier spectra monitored at four pairs of points symmetrically distanced relative to the $(X-Z)$ midplane for $\delta = 0.6$, $Ra = 1.4 \times 10^6$: (a) P1 and P5; (b) P2 and P6; (c) P3 and P7; (d) P4 and P8. The results were obtained on a 200^3 structured uniform grid.

Ra value each time by no more than 5%, followed by the continuous monitoring of the flow characteristics at 8 representative control points.

The slightly supercritical flows observed for all three configurations were characterized by spatio-temporal symmetry H relative to the $X-Z$ midplane and preserved the Y_2 symmetry group. For the configurations characterized by the values of $\delta = 0.4$ and 0.5, the Y_2 symmetry was preserved, but half a period apart. It was found that the distance between the vertical boundaries of the cubic enclosure and the surfaces of the cylinders plays a significant role in determining the spatio-temporal characteristics of the observed instabilities, which can be attributed to the stabilizing effect of the vertical boundaries on the oscillating flow. When reaching the top boundary of the cubic enclosure, the vertically rising thermal plume separated into two parts, after which the flow changed direction to horizontal. The abrupt change in the flow direction after the thermal plume separated when reaching the top boundary of the enclosure was the major source of instability observed in all the investigated flows.

Together with our previous study [21], the present work sheds light on the instability characteristics typical of constellations of immersed objects of fixed temperature confined in a constant-temperature

container. It addresses the impact of the object orientation and its closeness to container boundaries on the spatio-temporal symmetries of the obtained slightly supercritical flows. Moreover, the characteristics observed are not only restricted to the natural convection flows, but are also typical of shear-driven confined flows, as was elucidated in Ref. [32]. A common denominator determining characteristics of the observed instabilities is thus not necessarily related to the mechanism driving the flows but rather to their highly separated physics, typical of confined slightly supercritical flows. The current study thus constitutes an important milestone, which can be used for the further examination of linear stability analysis performed by the Arnoldi iteration applied to a linearized set of the governing equations (Eqs. (1)–(3)). This will be the focus of our future work.

Declaration of competing interest

The authors declare that they have no known competing financial interests or personal relationships that could have appeared to influence the work reported in this paper.

Acknowledgement

The study was partially funded by the Israeli Ministry of Energy and Infrastructure, under contract number: (3–15771) 218-11-038).

References

[1] X. Xia, K. Mohseni, Unsteady aerodynamics and vortex-sheet formation of two-dimensional airfoil, J. Fluid Mech. 830 (2017) 439–478.
[2] U. Pesavento, Z. Wang, Flapping wing flight can save aerodynamic power compared to steady flight, Phys. Rev. Lett. 103 (2009) 118102.
[3] J. Choi, T. Colonius, D.R. Williams, Surging and plunging oscillations of an airfoil at low Reynolds number, J. Fluid Mech. 763 (2015) 237–253.
[4] V. Terekhov, A. Chichidaev, A. Ekaid, Buoyancy heat transfer in staggered dividing square enclosure, Therm. Sci. 15 (2011) 409–422.
[5] A. Abidi-Saad, M. Kadja, C. Popa, G. Polidori, Effect of adiabatic square ribs on natural convection in an asymmetrically heated channel, Heat Mass Tran. 53 (2017) 743–752.
[6] V. Terekhov, A. Ekaid, K. Yassin, Laminar free convection heat transfer and separated flow structure in a vertical channel with isothermal walls and two adiabatic opposing fins, J. Eng. Thermophys. 26 (2017) 339–352.
[7] A. Saha, S. Chanda, Fully-developed natural convection in a periodic array of pin-fins, Int. J. Therm. Sci. 137 (2019) 325–336.
[8] S. Bhavnani, A. Bergles, Effect of surface geometry and orientation on laminar natural convection heat transfer from a vertical flat plane with transverse roughness elements, Int. J. Heat Mass Tran. 33 (1990) 965–981.
[9] M. Audin, Natural convection over a vertical flat plate in the presence of fins, Comm. Heat Mass Transf. 24 (1997) 521–531.
[10] G. Tanda, Natural convective heat transfer in vertical channels with low-thermal-conductivity fins, Int. J. Heat Fluid Flow 29 (2008) 1319–1325.
[11] V. Terekhov, V. Terekhov, Numerical investigation of heat transfer in tall enclosure within multiple fins attached to an active wall, Comput. Therm. Sci. 2 (2010) 33–42.
[12] T. Seta, Implicit temperature-correction-based immersed-boundary thermal lattice Boltzmann method for the simulation of natural convection, Phys. Rev. E (2013) 63304.
[13] F. Moukalled, S. Acharya, Natural convection in the annulus between concentric horizontal circular and square cylinders, J. Thermophys. Heat Tran. 10 (1996) 524–531.
[14] C. Shu, Y.D. Zhu, Efficient computation of natural convection in a concentric annulus between an outer square cylinder and an inner circular cylinder, Int. J. Numer. Methods Fluid. 38 (2002) 429–445.
[15] Y. Feldman, Semi-implicit direct forcing immersed boundary method for incompressible viscous thermal flow problems: a Schur complement approach, Int. J. Heat Mass Tran. 127 (2018) 1267–1283.
[16] Y. Park, M. Ha, C. Choi, J. Park, Natural convection in a square enclosure with two inner circular cylinders positioned at different vertical locations, Int. J. Heat Mass Tran. 77 (2014) 501–518.
[17] Y. Feldman, Oscillatory instability of 2D natural convection flow in a square enclosure with a tandem of vertically aligned cylinders, Fluid Dynam. Res. (2018), https://doi.org/10.1088/1873–7005/aab396 in press.
[18] Y.M. Seo, J.H. Doo, M.Y. Ha, Three-dimensional flow instability of natural convection induced by variation in radius of inner circular cylinder inside cubic enclosure, Int. J. Heat Mass Tran. 95 (2016) 566–578.
[19] Y.M. Seo, Y.G. Park, M. Kim, H.S. Yoon, M.Y. Ha, Two-dimensional flow instability induced by natural convection in a square enclosure with four inner cylinders. part i: effect of horizontal position of inner cylinders, Int. J. Heat Mass Tran. 113 (2017) 1306–1318.
[20] Y.M. Seo, G.S. Mun, Y.G. Park, M.Y. Ha, Two-dimensional flow instability induced by natural convection in a square enclosure with four inner cylinders. part ii: effect of various positions of inner cylinders, Int. J. Heat Mass Tran. 113 (2017) 1319–1331.
[21] A. Spizzichino, E. Zemach, Y. Feldman, Oscillatory instability of a 3d natural convection flow around a tandem of cold and hot vertically aligned cylinders placed inside a cold cubic enclosure, Int. J. Heat Mass Tran. 141 (2019) 327–345.
[22] G. Kefayati, H. Tang, Double-diffusive natural convection and entropy generation of Carreau fluid in a heated enclosure with an inner circular cold cylinder (Part I: Heat and mass transfer), Int. J. Heat Mass Tran. 120 (2018) 731–750.
[23] G. Kefayati, H. Tang, Lattice Boltzmann simulation of viscoplastic fluids on natural convection in an inclined enclosure with inner cold circular/elliptical cylinders (Part I: one cylinder), Int. J. Heat Mass Tran. 123 (2018) 1138–1162.
[24] G. Kefayati, H. Tang, MHD thermosolutal natural convection and entropy generation of Carreau fluid in a heated enclosure with two inner circular cold cylinders, using LBM, Int. J. Heat Mass Tran. 126 (2018) 508–530.
[25] S. Xin, P. Le Quéré, An extended Chebyshev pseudo-spectral benchmark for the 8:1 differentially heated cavity, Int. J. Numer. Methods Fluid. 40 (2002) 981–998.
[26] H. Vitoshkin, A.Y. Gelfgat, On direct inverse of Stokes, Helmholtz and Laplacian operators in view of time-stepper-based Newton and Arnoldi solvers in incompressible CFD, Commun. Comput. Phys. 14 (2013) 1103–1119.
[27] S.V. Patankar, Numerical Heat Transfer and Fluid Flow, McGraw-Hill, 1980.
[28] R. Warrington, R. Powe, The transfer of heat by natural convection between bodies and their enclosures, Int. J. Heat Mass Tran. 28 (1985) 319–320.
[29] Y. Feldman, A.Y. Gelfgat, Oscillatory instability of a three-dimensional lid-driven flow in a cube, Phys. Fluids 22 (2010) 93602.
[30] Y. Gulberg, Y. Feldman, Flow control through use of heterogeneous porous media: smart passive thermo-insulating materials, Int. J. Therm. Sci. 110 (2016) 369–382.
[31] Y.A. Kuznetsov, Elements of Applied Bifurxation Theory, Second Edition, Volume 112 of Applied Mathematical Sciences, Springer, 1998, pp. 273–288.
[32] Y. Feldman, Theoretical analysis of three-dimensional bifurcated flow inside a diagonally lid-driven cavity, Theor. Comput. Fluid Dynam. 29 (2015) 245–261.